MATERIALS SCIENCE

Indoor photovoltaics awaken the world's first solar cells

Bin Yan[1,2]†, Xinsheng Liu[3]†, Wenbo Lu[1,4], Mingjie Feng[1,5], Hui-Juan Yan[1,4], Zongbao Li[6], Shunchang Liu[1], Cong Wang[2], Jin-Song Hu[1,4], Ding-Jiang Xue[1,4]*

Copyright © 2022 The Authors, some rights reserved; exclusive licensee American Association for the Advancement of Science. No claim to original U.S. Government Works. Distributed under a Creative Commons Attribution NonCommercial License 4.0 (CC-BY).

Selenium (Se) solar cells were the world's first solid-state photovoltaics reported in 1883, opening the modern photovoltaics. However, its wide bandgap (~1.9 eV) limits sunlight harvesting. Here, we revisit the world's oldest but long-ignored photovoltaic material with the emergence of indoor photovoltaics (IPVs); the absorption spectrum of Se perfectly matches the emission spectra of commonly used indoor light sources in the 400 to 700 nm range. We find that the widely used Te adhesion layer also passivates defects at the nonbonded Se/TiO_2 interface. By optimizing the Te coverage from 6.9 to 70.4%, the resulting Se cells exhibit an efficiency of 15.1% under 1000 lux indoor illumination and show no efficiency loss after 1000 hours of continuous indoor illumination without encapsulation, outperforming the present IPV industry standard of amorphous silicon cells in both efficiency and stability. We further fabricate Se modules (6.75 cm^2) that produce 232.6 μW output power under indoor illumination, powering a radio-frequency identification–based localization tag.

INTRODUCTION

After Willoughby Smith discovered the photoconductivity of selenium (Se) in 1873, Charles Fritts constructed the first solid-state solar cells in 1883 by sandwiching Se film between a metal foil and a thin gold (Au) layer (*1*). Despite the low preliminary power conversion efficiency (PCE) of <1%, these early discoveries initiated the research of photovoltaic field and then inspired the emergence of silicon (Si) solar cells in 1954 (*2*), thus laying the foundation for modern photovoltaic industry. However, compared with the suitable bandgap of Si (~1.12 eV) for single-junction solar cells, an obvious drawback of Se for photovoltaic applications is its wide bandgap of ~1.9 eV (*3*). This is too large for the use as a single-absorber photovoltaic device, exhibiting a low Shockley-Quiesser (S-Q) efficiency limit of ~23% under AM1.5G illumination (*1*, *4*). Se solar cells thereby declined as the rapid development of Si photovoltaic industry.

Until recently, with the advent of the Internet of Things (IoT), indoor photovoltaics (IPVs) that convert indoor light into usable electrical power have been recognized as the most promising energy supplier for the wireless devices including actuators, sensors, and communication devices connected and automated by IoT technology (*5*, *6*). The narrow emission spectra ranging from 400 to 700 nm of the commonly used indoor light sources such as light-emitting diodes (LEDs) and fluorescent lamps (FLs) thereby determine that the optimal bandgap of indoor light absorber materials is ~1.9 eV (*7*, *8*). This hence leads us to reconsider the oldest photovoltaic material of Se, wherein its wide bandgap of ~1.9 eV makes it an ideal candidate for IPVs.

Another notable advantage of Se for IPVs is its minimal toxicity risk considering the small applied quantities in IPVs (~0.48 mg cm^{-2} for Se films with a thickness of 1 μm), wherein only large doses of Se intake result in potential toxicity in humans (*9*). Se has been well established for several decades as an essential element for humans that is beneficial to the immune system (*10*). This satisfies the requirement of IPV applications, where the regulation of materials used to manufacture IoT products would be strictly governed by the restrictions on the use of certain hazardous substances (RoHS) legislation (*11*, *12*). In addition, the excellent inherent stability of Se to ambient conditions such as oxygen and humidity ensures its stable photovoltaic performance in indoor environments (*10*). However, the photovoltaic performance of Se cells under indoor light conditions has not been systematically investigated so far, despite the recent rapid efficiency improvement in Se solar cells under standard sunlight (*1*, *2*, *13*).

Here, we demonstrate the unique advantages of Se for IPVs: suitable wide bandgap (~1.9 eV) enabling high indoor S-Q limit of above 55%, high absorption coefficient (above 10^5 cm^{-1}), low-temperature film process arising from its low crystallization temperature (121°C), simple composition, nontoxicity in the small applied quantities in IPVs, and intrinsic environmental stability. We then unveil the underexplored effect of a widely used Te layer that not only provides a bridge bonding between Se and TiO_2 layers but also passivates trap states at the nonbonded Se/TiO_2 interface. We therefore optimize the coverage of the Te layer atop the TiO_2 layer, achieving an efficiently passivated Se/TiO_2 interface. The resulting Se cells exhibit a PCE of 15.1% under 1000 lux indoor illumination and show no performance degradation after 1000 hours of continuous indoor illumination without encapsulation, outperforming the market-dominating amorphous silicon (a-Si) cells—the industry standard for IPVs—in both PCE and stability. We further fabricate Se modules (6.75 cm^2) that produce 232.6 μW output power under 1000 lux indoor illumination, powering a typical IoT wireless device of radio-frequency identification (RFID)–based localization tag.

[1]Beijing National Laboratory for Molecular Sciences (BNLMS), CAS Key Laboratory of Molecular Nanostructure and Nanotechnology, Institute of Chemistry, Chinese Academy of Sciences, Beijing 100190, China. [2]Beijing Key Lab of Microstructure and Properties of Advanced Materials, Faculty of Materials and Manufacturing, Beijing University of Technology, Beijing 100124, China. [3]Key Laboratory for Special Functional Materials of Ministry of Education, Henan University, Kaifeng 475004, China. [4]University of Chinese Academy of Sciences, Beijing 100049, China. [5]National Engineering Research Center for Advanced Polymer Processing Technology, Zhengzhou University, Zhengzhou 450002, China. [6]School of Material and Chemical Engineering, Institute of Cultural and Technological Industry Innovation of Tongren, Tongren University, Tongren 554300, China.
†These authors contributed equally to this work.
*Corresponding author. Email: djxue@iccas.ac.cn

RESULTS

Advantages of Se for IPVs

With the emergence of low power–consuming wireless protocols used in IoT ecosystem including RFID tags, long-range radio (LoRa) backscatter, passive Wi-Fi, Bluetooth low energy, ANT, and Zigbee (Fig. 1A) (*6*, *12*), powering such IoT devices by harvesting indoor light via IPV cells is becoming possible. Specially, 10 cm^2 IPVs with an indoor PCE of 15% under 1000 lux illumination of LEDs (~300 μW cm^{-2}) can produce ~0.45 mW output power, thus operating many IoT devices. IPVs thereby become a growing research field, where various types of PV technologies including dye-sensitized solar cells (*14*, *15*), organic photovoltaics (*16*, *17*), and lead-halide perovskite solar cells (*18*–*20*) have been explored for IPVs measured under indoor light sources including LEDs and FLs.

The indoor artificial light is usually designed on the basis of the sensitivity of human eyes, implying that the emission spectra of commonly used indoor light sources should be mostly within visible region ranging from 400 to 700 nm *(16)*. This is much narrower than the standard solar spectrum (AM1.5G) (Fig. 1B). The design principle of IPVs should be thereby different from that of conventional outdoor photovoltaics. We then compared the S-Q limits under standard solar irradiance and indoor illumination from a 2700 K LED and an FL (Fig. 1C), according to previous reports (*7*, *21*). Compared with the optimal bandgap of 1.3 to 1.5 eV for the standard solar irradiance (*21*), the optimum bandgap for indoor light sources is 1.8 to 1.9 eV, which induces the maximum S-Q limits of 56 and 57% for LED and FL (*7*), respectively. These higher S-Q limits under indoor light are attributed to the narrow emission spectra of indoor light sources compared to that under the standard solar spectrum; this leads to the easy absorption of all indoor light photons.

The optimal bandgap of ~1.9 eV for indoor light harvesting enables us to reconsider the world's oldest photovoltaic material of Se with an attractive bandgap of ~1.9 eV, although it has been ignored for a long time because of its unsuitable wide bandgap for standard solar irradiation. The absorption spectrum of Se films perfectly matches that of indoor light sources (Fig. 1D), inducing high S-Q limits (>55%) under indoor illumination. Se also has a high optical absorption coefficient (greater than 10^5 cm^{-1}) due to its direct optical transition (Fig. 1E). In addition, low crystallization temperature of amorphous Se (121°C) induces the low-temperature processing of Se films (Fig. 1F), endowing the high-temperature compatibility with most flexible substrates such as polyimide and poly(ethylene terephthalate). The combination of high absorption coefficient and low-temperature film process thereby allows the fabrication of flexible Se thin-film photovoltaic cells, thus enabling the easy integration with IoT devices. In summary, the above features of Se, combined with aforementioned nontoxicity and excellent stability, make Se ideal for IPV applications.

Comparison of PV performances under AM1.5G and indoor light conditions

We then adopted a widely used superstrate configuration of glass/F-doped tin oxide (FTO)/TiO_2/tellurium (Te)/Se/Au to fabricate Se thin-film solar cells (Fig. 2A). Environmentally friendly TiO_2 was

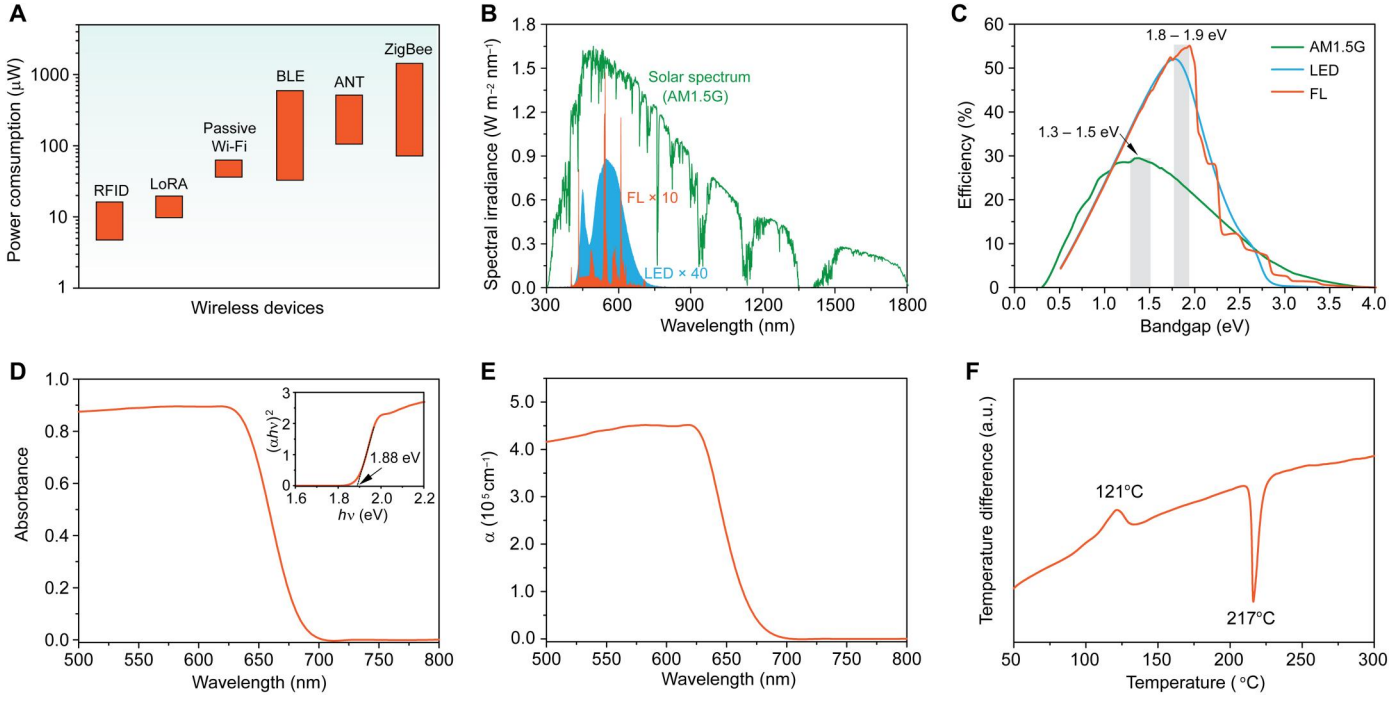

Fig. 1. Analysis of Se for indoor photovoltaics. (**A**) Power consumption of wireless protocols used in IoT ecosystem. (**B**) Comparison of the emission spectra of AM1.5G solar, a 2700 K LED, and an FL recorded at 1000 lux. The spectral intensities of LED and FL were amplified by 40 and 10 times for clear showing. (**C**) Bandgap-dependent S-Q limits under illumination from one sun, an LED, and an FT at 1000 lux, respectively. Adapted with permission from ref 7. Copyright 2019, Wiley-VCH Verlag. (**D**) Absorption spectrum of Se film. Inset: Tauc plot for Se film to determine the bandgap of Se. (**E**) Wavelength-dependent absorption coefficient of Se. (**F**) DTA of amorphous Se powder at a ramp rate of 5°C min^{-1} in a N_2 flowing environment.

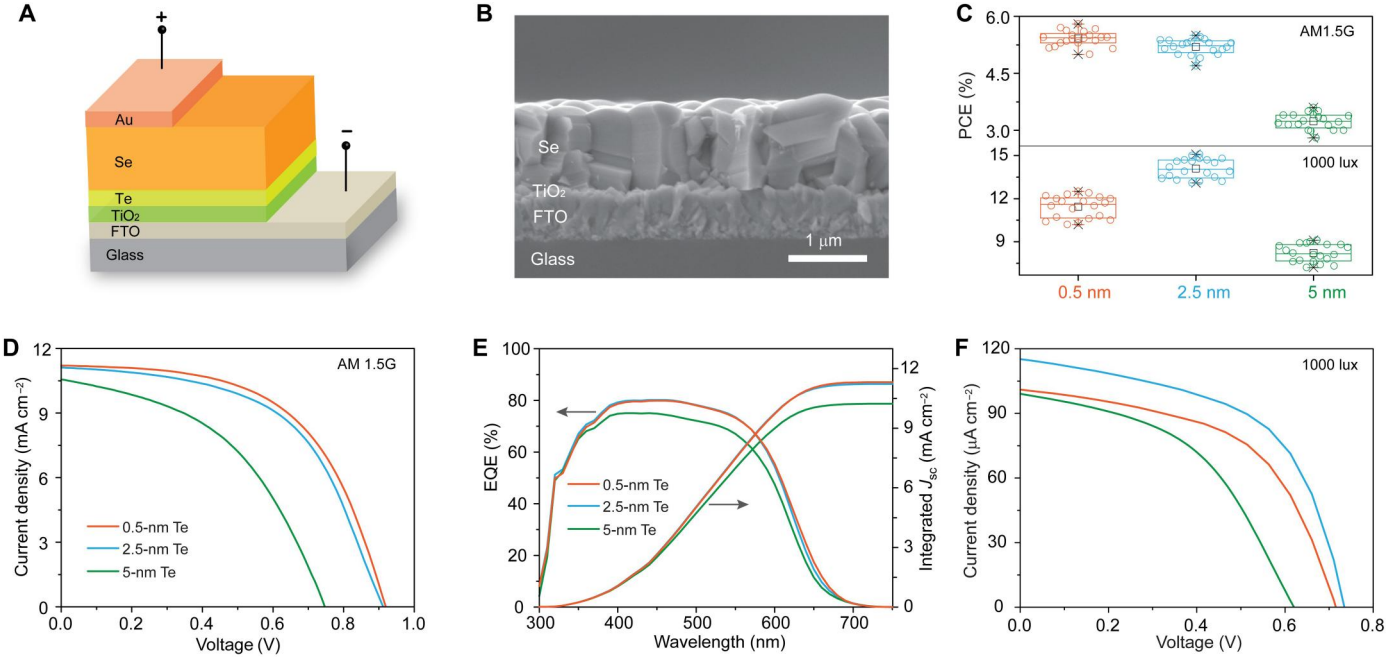

Fig. 2. Photovoltaic performances of Se cells measured under AM1.5G and indoor light conditions. (**A**) Schematic of Se thin-film solar cell architecture. (**B**) Cross-sectional SEM image of Se cell. (**C**) PCE statistics of 20 Se cells for 0.5-, 2.5-, and 5-nm Te layers measured under AM1.5G and indoor illumination of 1000 lux. (**D**) *J-V* curves of 0.5, 2.5, and 5 nm Te layer Se devices under standard one-sun illumination. (**E**) EQE curves of 0.5, 2.5, and 5 nm Te layer Se devices. (**F**) *J-V* curves of 0.5, 2.5, and 5 nm Te layer Se devices under indoor illumination of 1000 lux.

selected as the buffer layer, thus achieving the construction of non-toxic Se-based devices. This is especially significant for the indoor environment application, where the only one barrier from the encapsulation layer between the toxic functional layers and the human end-user still poses significantly higher exposure risks in case of damage to the device in an indoor setting.

We also employed a widely used Te layer serving as an adhesion layer between TiO_2 and Se to improve the adhesion and uniformity of Se films. Te layers were deposited onto the TiO_2 layer before Se deposition. Guided by the Te thickness window for optimized PCEs of Se solar cells under standard AM1.5G illumination, we sought to fabricate high-performance Se IPV cells with different Te thicknesses of 0.5, 2.5, and 5 nm. The thickness of Se films keeps the same thickness of 1 μm for all devices (Fig. 2B), which is thick enough to absorb most of the incident light due to the high absorption coefficient of Se. Au electrodes were subsequently deposited onto Se films by thermal evaporation. The devices were finally completed by annealing at 200°C for 2 min in air (fig. S1).

We first characterized the Se solar cells under standard one-sun illumination (AM1.5G, 100 mW cm^{-2}). Figure 2C shows the statistical photovoltaic performance of the Se solar cells with different thickness of the Te layer. The three types of Se devices exhibit average PCEs of 5.5% for 0.5 nm Te devices, 5.2% for 2.5 nm Te devices, and 3.2% for 5 nm Te devices. No hysteresis between forward and reserve scans was observed in these Se devices (fig. S2) arising from the strong covalency of Se—Se bonds (*10*). This is superior to the highly ionic perovskite solar cells exhibiting current density–voltage (*J-V*) hysteresis (*22*, *23*). The best-performing devices of each type show AM1.5G PCEs of 5.8, 5.5, and 3.6% (Fig. 2D and table S1). Our 0.5 nm Te devices achieve the highest PCE reported among TiO_2/Se heterojunction solar cells. The integrated current densities from the external quantum efficiency (EQE) spectra agree well with the short-circuit current density (J_{sc}) values measured from *J-V* characterization (within 5% deviation) (Fig. 2E). These results are consistent with the previous reports —the thicker Te layer, the poorer performance—arising from the narrow bandgap of Te (0.35 eV) and the lower shunt resistance as well as larger leak current along the device when increasing the Te thickness (*2*).

We next measured the IPV performances of these Se devices under indoor illumination at 1000 lux, wherein the commonly used LED (2700 K) was used as light source to simulate the indoor illumination environment. Unexpectedly, the photovoltaic performances of Se cells with 0.5 and 2.5 nm Te are reversed under indoor condition compared to the one-sun condition (Fig. 2C). The 2.5 nm Te devices exhibit higher average indoor PCEs of 14.1% than that of the 0.5 nm Te devices (11.4%), wherein the 5 nm Te devices still show the lowest indoor PCEs (8.2%) similar to their one-sun performances. Representative *J-V* curves and photovoltaic parameters of each type device are shown in Fig. 2F and table S2, respectively. The above results indicate that the optimization of PV devices for one-sun irradiation may not be optimized for indoor light conditions.

Investigation of the effect of Te layer

This contrary tendency between one-sun and indoor performances of 0.5 and 2.5 nm Te devices led us to posit that the optimal thickness of the Te layer for one-sun condition is different from that for indoor light conditions, considering the identical thickness of Se and TiO_2 layers. This can be attributed to significantly different

light intensities between indoor light and sunlight, in addition to different emission spectra (*8*); indoor light has a very weak intensity, typically 0.1 to 1% of the standard AM1.5G condition (Fig. 1B). Such low injection level could only generate a relatively small number of carriers. We thereby reasoned that most of the photogenerated carriers would be trapped at the Se/TiO_2 interface arising from the higher ratio of trapped carriers to photogenerated carriers (Fig. 3A), resulting in trap-assisted recombination losses. This is in contrast with the numerous photogenerated carriers under one-sun condition, which are much higher than the Se/TiO_2 interfacial traps. The excited electrons would fill all the trap states at the Se/TiO_2 interface (Fig. 3B) and lead to a positive photodoping effect, thus eliminating the nonradiative recombination centers (*24*–*26*).

Understanding the effect of the Te layer on the interfacial trap states at the Se/TiO_2 interface is thereby crucial for the further optimization of Se solar cells under indoor conditions. However, despite a long history of Te usage and a critical role in fabricating high-quality Se films that avoids the peeling of Se film from substrates during and after the annealing process (fig. S3), the detailed mechanism of Te remains unclear. The conventionally supposed view was only that the Te layer provided nucleation sites for Se, thus improving the Se adhesion and leading to a good morphology of trigonal Se films (*1*, *2*), whereas the effect of Te on the Se/TiO_2 interfacial trap states as well as the interaction between Te and TiO_2 have still not been reported so far.

We focused therefore on the interaction of Te between Se and TiO_2 layers. We reasoned that Te would act as a bridge between Se and TiO_2 layers. First, Se and Te atoms as group VI elements are prone to form $Se_{1-x}Te_x$ alloy because of their same one-dimensional crystal structure (*27*). Se and Te atoms can be strongly connected via covalent bonds in a single helical chain (Fig. 3C). Next, we applied density functional theory (DFT) to investigate the interaction between Te and TiO_2, where the interaction between Se and TiO_2 was also studied for comparison. When we deposited a Te and Se alloy chain onto a preferred [101]-orientation TiO_2 layer (fig. S4), we found that the bonding energy of Te-Se and TiO_2 (−0.73 eV per Se chain) is far lower than that of Se and TiO_2 (−0.06 eV per Se chain) (Fig. 3, C and D). This is attributed to the different Pauling electronegativities of O (3.44), Se (2.55), and Te (2.01) (*28*), thus enabling the easy formation of Te—O bonds but the difficulty in Se—O bonds (fig. S5). The above calculated results confirm the strong bonding between Te and TiO_2 via Te—O bonds but the weak interaction between Se and TiO_2. This provides an explanation for the indispensable addition of Te adhesion layer during the deposition of Se films on TiO_2 substrates.

To verify the Te—O bond at the TiO_2/Te interface from experiment, we carried out x-ray photoelectron spectroscopy (XPS) measurements on the Te film deposited atop the TiO_2 layer. To avoid the possible influence of oxygen from ambient air, the thickness of the Te layer was reached to about 70 nm (fig. S6). We first performed the XPS measurement on the top surface of Te/TiO_2 film, where the Te 3d core level from the top of Te/TiO_2 film is fit to four peaks (Fig. 3E). Two main peaks located at 573 eV (Te $3d_{5/2}$) and 584 eV (Te $3d_{3/2}$) correspond to elemental Te. Two additional weaker peaks, which shifted to higher binding energies at 576 and 588 eV compared with Te $3d_{5/2}$ and Te $3d_{3/2}$ peaks in elemental Te, are attributed to Te^{4+} in TeO_2. This indicates the easy oxidation of Te to TeO_2 in ambient air. In contrast, Se films shows high air stability, where no peak corresponding to +4 state of Se is observed (fig. S7). This indicates that Se atoms are more difficult to bond with O atoms compared with Te atoms, thus resulting in the peeling of Se film from TiO_2 substrates during and after the annealing process. We

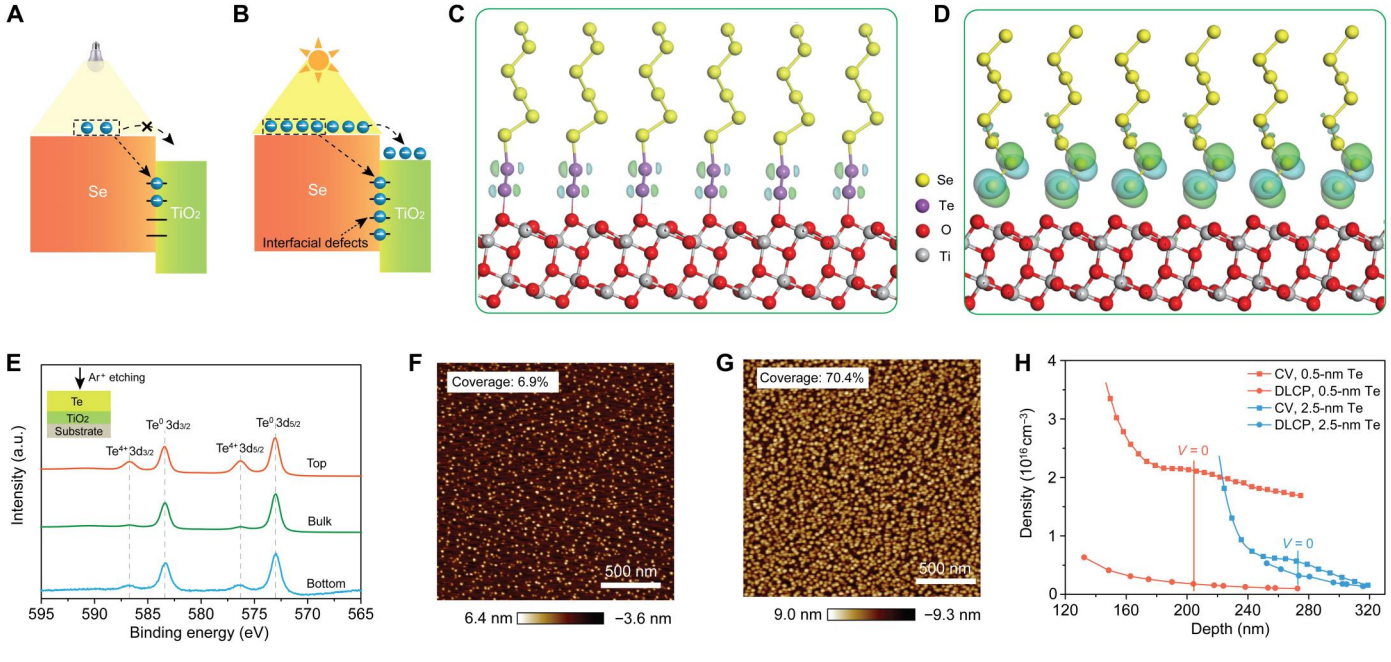

Fig. 3. Investigation of the effect of Te on interface quality between Se and TiO_2. Comparison of the operational mechanism between (**A**) indoor condition and (**B**) one-sun condition. DFT models for (**C**) delocalized surface defects at the Te-modified Se/TiO_2 interface and (**D**) localized surface defects at the Se/TiO_2 interface. (**E**) XPS spectra of Te 3d recorded during sputtering from the top to the bottom of Te film. a.u., arbitrary unit. AFM images of (**F**) 0.5 nm and (**G**) 2.5 nm Te layers. (**H**) *C-V* and DLCP characteristics of 0.5 nm Te and 2.5 nm Te devices.

next etched the Te film for about 30 nm by Ar^+ (fig. S8). Only Te^0 3d peaks from elemental Te are found, where the Te^{4+} 3d peaks are negligible. Yet, as further etching the Te film for about 30 nm, in addition to the consistent Te^0 3d peaks, Te^{4+} 3d peaks reappear, thus confirming the formation of Te—O bond at the TiO_2/Te interface.

Given the bridge bonding of Te with Se and TiO_2 layers, we reasoned that Te not only provides the reported interfacial adhesion effect for Se and TiO_2 layers but also may passivate the interfacial defects at the Se/TiO_2 interface induced by the nonbonding between Se and TiO_2. DFT further reveals that the dangling bonds on the surface of Se chain lead to localized states inside the bandgap (Fig. 3D), resulting in recombination losses. In contrast, the interfacial trap states become more delocalized with lower density when incorporating Te between Se and TiO_2 layers (Fig. 3C), thus indicating the passivation effect of Te at the Se/TiO_2 interface.

The coverage of Te on the surface of substrates thereby determines the degree of surface passivation. We then applied atomic force microscopy (AFM) to characterize the coverage of Te layers with different thickness (0.5, 2.5, and 5 nm) on substrates. Figure 3F shows that the 0.5nm Te layer exhibits a noncontinuous film with isolated Te islands, demonstrating a coverage of about 6.9% (fig. S9). In contrast, the 2.5 and 5 nm Te form nearly continuous layers with coverages of 70.4 and 75.8% (Fig. 3G and figs. S10 and S11), which are an order of magnitude higher than that of 0.5 nm Te. The combination of scanning electron microscopy (SEM) and energy-dispersive X-ray spectroscopy (EDS) mapping measurements further confirms the higher coverage of 2.5 and 5 nm Te compared with 0.5 nm Te (fig. S12). The above results thus indicate that the minimum thickness of Te achieving high coverage on substrates is about 2.5 nm, because excess Te can harm the device performance arising from its narrow bandgap of 0.35 eV and the lower shunt resistance (*3*, *27*).

To experimentally evaluate the degree of surface passivation of the Se/TiO_2 interface by Te, we then applied a combination of drive-level capacitance profiling (DLCP) and capacitance-voltage (*C-V*) profiling measurements on the 0.5 and 2.5 nm Te devices. DLCP measurements are sensitive to free carriers and bulk defects; *C-V* measurements are responsive to free carriers as well as bulk and interfacial defects (*29*). The density of interfacial defects at the heterojunction is thereby obtained by subtracting defect density calculated from DLCP (N_{DLCP}) from defect density calculated from *C-V* ($N_{C\text{-}V}$). Figure 3H shows that the 2.5 nm Te devices exhibit sixfold lower interfacial defect density (6.5×10^{11} cm^{-2}) than do the 0.5 nm Te devices (3.9×10^{12} cm^{-2}), which is further confirmed by the average and SD of those values (fig. S13). This is attributed to the higher coverage of the 2.5 nm Te layer that provides complete surface passivation compared with that of 0.5 nm Te supplying incomplete passivation, thus explaining why the 2.5 nm Te devices exhibit higher indoor efficiency than do the 0.5 nm Te devices. Overall, incorporating Te at the Se/TiO_2 interface provides synthetic effect of strong bonding between Se and TiO_2 as well as surface passivation.

Application in powering IoT wireless devices

We further investigated the IPV performances of the optimized 2.5 nm Te devices at 200, 500, and 1000 lux illuminances, which represent the typical indoor light conditions from dim living room

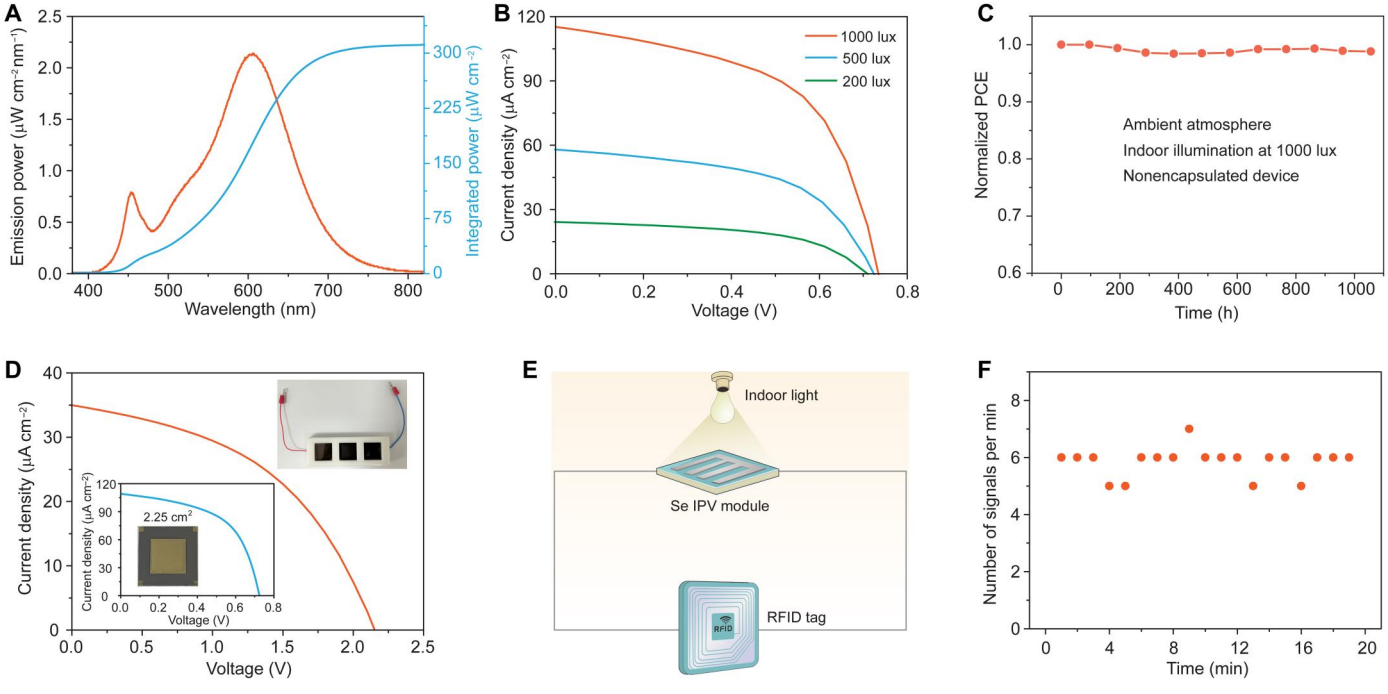

Fig. 4. Application in powering IoT wireless device. (**A**) Emission power and integrated power spectra of a 2700 K LED at 1000 lux. (**B**) *J-V* curves of 2.5 nm Te device under illumination at 200, 500, and 1000 lux. (**C**) Evolution of normalized PCEs of unencapsulated Se device under continuous indoor illumination at 1000 lux in an ambient atmosphere. (**D**) *J-V* curves of individual large-area (2.25 cm^2) Se device and (3×2.25 cm^2) module under indoor illumination at 1000 lux. Inset: Photographs of individual large-area Se cell and module. (**E**) Schematic of self-powered RFID-based localization tag enabled by Se module under indoor light illumination. (**F**) Measured number of signals per minute from a Se module–powered RFID tag.

through library to bright supermarket (*30*). The corresponding input light power densities at 200, 500, and 1000 lux were measured to be 63.9, 156.4, and 310.4 μW cm^{-2} by a spectrometer (Fig. 4A and fig. S14), while all IPV measurements were put in a black box to prevent the interference of stray light, according to a reliable measurement method for IPVs reported by Hou and coworkers (*31*).

Figure 4B shows the *J-V* curves and the corresponding photovoltaic parameters under the three illumination conditions (fig. S15 and table S3). The devices exhibited PCEs of 14.3, 14.5, and 15.1% under the indoor illumination at 200, 500, and 1000 lux, respectively. Notably, the PCE values under indoor illumination correspond to about threefold increase with respect to their PCEs under one-sun illumination, demonstrating the perfect match of Se absorption spectrum with indoor light sources. We further tested the stability of Se devices under indoor illumination and ambient conditions. The unencapsulated devices show negligible PCE loss after 1000 hours of continuous indoor illumination in ambient atmosphere at room temperature and a relative humidity of 50 to 85% (Fig. 4C), which can be attributed to the high stability of Se layer arising from its strong covalent character (*10*, *32*).

The Se cells thereby outperform market-dominating a-Si cells as present industry standard for IPVs in both PCE and stability, where commercial a-Si cells usually exhibit indoor PCEs below 10% with relatively poor photostability due to the well-known Staebler-Wronski effect (*6*, *33*, *34*). In addition, despite the relatively lower indoor PCEs of Se cells compared to wide-bandgap lead halide perovskite devices, the intrinsic environmental stability and nontoxicity of Se is superior to that of perovskites with moisture-induced degradation and in-migration–related hysteresis as well as water-soluble toxic lead (*35*–*37*), especially in the indoor environment, where the probable lead leakage would cause direct threat to human end-user health. The above results thus indicate that Se is an attractive alternative candidate for IPV absorber.

We finally sought to demonstrate the ability of our Se devices to power IoT wireless devices. Specifically, as a proof of concept, we used an RFID-based localization tag that provides accurate indoor positioning services through the measurement of signal strength of RF signals transmitted from tags and received by an RFID reader (*38*, *39*). Operating this RFID tag through an external power source requires an input voltage of above 1.5 V and an average input power of tens of microwatts. To achieve such voltage and power from our Se cells under indoor light illumination, we fabricated large-area Se cells (2.25 cm^2) and then connected three cells in series through external wiring to construct Se modules. The single large-area Se cell exhibits a PCE of 14.0% under indoor illumination (2700 K LED, 1000 lux, 310.4 μW cm^{-2}), with an open-circuit voltage (V_{oc}) of 0.72 V, short-circuit current (J_{sc}) of 0.109 mA cm^{-2}, and fill factor (FF) of 55.3% (Fig. 4D and fig. S16), comparable to that of small-area (0.09 cm^2) Se devices, indicating the high uniformity of as-deposited Se films. The Se module (3 × 2.25 cm^2) achieves a PCE of 11.1% with a V_{oc} of 2.1 V under 1000 lux indoor illumination that produces 232.6 μW output power (Fig. 4D). This is enough to power the RFID tag when illuminated by indoor light (Fig. 4E). Figure 4F shows that RF signals were emitted from this Se module–powered RFID tag, thus demonstrating the great potential of wide-bandgap Se cells for powering the IoT wireless devices.

DISCUSSION

In summary, we revisit the world's oldest photovoltaic material of Se with the emergence of IPVs arising from its unique advantages: suitable wide bandgap for indoor light harvesting, high absorption coefficient, low-temperature film process, simple composition, nontoxicity in the applied quantities in IPVs, and intrinsic environmental stability. We found the synthetic effect of the Te layer on high-performance Se cells that improved the adhesion between Se and TiO_2 and passivated the Se/TiO_2 interfacial trap states. By optimizing the coverage of the Te layer, we achieved a PCE of 15.1% for Se cells under 1000 lux indoor illumination, surpassing the present IPV industry standard of a-Si cells with indoor efficiencies below 10%. Unencapsulated Se devices exhibited no performance degradation after 1000 hours of continuous indoor illumination at 1000 lux. We further fabricated Se modules (3 × 2.25 cm^2) that produced a 232.6 μW output power under 1000 lux indoor illumination, powering an RFID-based localization lag. This study demonstrates the great potential of Se for IPVs as well as IoTs, regaining Se as an attractive absorber for photovoltaics.

MATERIALS AND METHODS

Device fabrication

All devices were deposited on an FTO conductive glass, which was ultrasonically cleaned using detergent, acetone, and isopropanol for 40 min each. TiO_2 buffer layer was deposited onto FTO glass sitting on a 450°C hotplate in air ambient by spray pyrolysis, where a mixed solution of titanium diisopropoxide bis(acetylacetonate) (75% weight % in isopropanol, Alladin) and absolute ethanol in the ratio of 1:9 by volume was used as a precursor. The mass fraction of titanium diisopropoxide bis(acetylacetonate) in the final mixed solution is 9.2%; the film was followed by an annealing at 500°C for 30 min and cooled down naturally. Te and Se (99.999%, Alfa Aesar) films were deposited on FTO/TiO_2 substrates by thermal evaporation (Beijing Technol Science) under a vacuum pressure of 8 × 10^{-4} Pa. After that, Au back-contact electrodes (70 nm) were deposited using a thermal evaporation system (Beijing Technol Science) through a shadow mask (0.09 cm^2) under a vacuum pressure of 6 × 10^{-4} Pa. Last, devices were completed by annealing at 200°C for 2 min under ambient conditions. The temperature accuracy of the hotplate was monitored by Hioki memory Hilogger LR8431-30 (fig. S17).

Material characterization

The optical absorbance of Se film was measured using an ultraviolet–visible–near-infrared spectrophotometer (UH4150, Hitachi). Differential thermal analysis (DTA) of amorphous Se powder was characterized at a ramp rate of 5°C min^{-1} in a N_2 flowing environment by PerkinElmer Instruments, Diamond TG/DTA6300. SEM images and EDS mapping were obtained with a Hitachi S-4800 microscope. AFM data were collected on a Bruker Dimension Icon microscope. High-resolution XPS measurements were performed on an ESCALab220i-XL electron spectrometer (VG Scientific) using 300-W Al Kα radiation. Powder X-ray diffraction patterns were recorded using a Rigaku D/Max-2500 diffractometer with a Cu target (Kα1 radiation, λ = 1.54056 Å).

Device performance characterization

J-V curves of the solar cells were obtained using an AM1.5G solar simulator (Newport, USA) equipped with a Keithley 2420 source meter and 450-W xenon lamp (OSRAM) in air at room temperature. Light intensity was adjusted using an National Renewable Energy Laboratory (NREL)-certified Si solar cell with a KG-2 filter for approximating AM1.5G light (100 mW cm^{-2}). The emission spectrum, light intensity, and illumination of the indoor light source of warm white 2700 K LED were measured with a high-precision fiber-optic spectrometer (Maya2000 Pro, Ocean Optics). The spectrometer was calibrated on 12 November 2021 by B. Hays in compliance with U.S. National Institute of Standards and Technology practices recommended in the NIST Handbook 150-2E, Technical Guide for Optical Radiation Measurements. The optical resolution of the spectrometer was about 1.1 nm, wherein the spectral wavelength accuracy was ±1.4 nm. All the spectral measurements were carried out by the spectrometer calibrated within 1 year. The measurement was performed in a homemade testing box in which all parts are painted black, while a baffle plate was designed to eliminate the effects from any stray lights according to a previous report (*31*). The active area was determined by the aperture shade mask (0.09 cm^2) placed in front of the glass side of solar cells to eliminate the edge effect. The *J-V* curves were measured with a scanning rate of 100 mV s^{-1} (voltage step of 20 mV and delay time of 200 ms). Both forward (−1 to 1 V) and backward (1 to −1 V) scans were recorded. EQE was measured at 0-V dc bias with a lock-in amplifier. Light source was generated with a 300-W xenon lamp of Newport (Oriel, 69911, Newport Corporation, Irvine, CA, USA) and then was split into specific wavelength using a Newport Oriel cornerstone 130 1/8 monochromator (Oriel, model 74004, Newport Corporation, Irvine, CA, USA). The stability test was carried out under continuous indoor illumination of 1000 for 1000 hours, where the device was stored in ambient atmosphere at room temperature and a relative humidity of 50 to 85%. The *C-V* curves and DLCP spectra were obtained using a Keithley 4200 sourcemeter. *C-V* measurements were performed at room temperature in an electromagnetic shielding box at a frequency of 10 kHz and an ac amplitude of 30 mV. The dc bias voltage was scanned from −1.0 to 0.5 V with a step size of 0.01 V. DLCP measurements were performed with an a.c. amplitude ranging from 14 to 140 mV and d.c. bias voltage from −0.2 to 0.2 V. The charge density was obtained by the relevant relations described in previous work (*40*).

Calculation methods

The crystal structures and electronic structures of Se and TiO_2 were calculated using plane-augmented wave scheme combined with pure GGA functional PBE used in the ab initio code VASP (*41*). An energy cutoff of 400 eV and a 2 × 2 × 1 *k*-point sampling of the first Brillouin zone were used (*42*). The convergence criterion regarding forces was set to 0.01 eV $Å^{-1}$ due to high computational costs.

Supplementary Materials

This PDF file includes:

Figs. S1 to S17

Tables S1 to S3

REFERENCES AND NOTES

1. T. K. Todorov, S. Singh, D. M. Bishop, O. Gunawan, Y. S. Lee, T. S. Gershon, K. W. Brew, P. D. Antunez, R. Haight, Ultrathin high band gap solar cells with improved efficiencies from the world's oldest photovoltaic material. *Nat. Commun.* **8**, 682 (2017).
2. I. Hadar, T.-B. Song, W. Ke, M. G. Kanatzidis, Modern processing and insights on selenium solar cells: The world's first photovoltaic device. *Adv. Energy Mater.* **9**, 1802766 (2019).
3. C. Tan, M. Amani, C. Zhao, M. Hettick, X. Song, D.-H. Lien, H. Li, M. Yeh, V. R. Shrestha, K. B. Crozier, M. C. Scott, A. Javey, Evaporated Se_xTe_{1-x} thin films with tunable bandgaps for short-wave infrared photodetectors. *Adv. Mater.* **32**, 2001329 (2020).
4. M. Zhu, F. Hao, L. Ma, T.-B. Song, C. E. Miller, M. R. Wasielewski, X. Li, M. G. Kanatzidis, Solution-processed air-stable mesoscopic selenium solar cells. *ACS Energy Lett.* **1**, 469–473 (2016).
5. R. Haight, W. Haensch, D. Friedman, Solar-powering the Internet of Things. *Science* **353**, 124–125 (2016).
6. I. Mathews, S. N. Kantareddy, T. Buonassisi, I. M. Peters, Technology and market perspective for indoor photovoltaic cells. *Joule* **3**, 1415–1426 (2019).
7. M.-J. Wu, C.-C. Kuo, L.-S. Jhuang, P.-H. Chen, Y.-F. Lai, F.-C. Chen, Bandgap engineering enhances the performance of mixed-cation perovskite materials for indoor photovoltaic applications. *Adv. Energy Mater.* **9**, 1901863 (2019).
8. M. H. Ann, J. Kim, M. Kim, G. Alosaimi, D. Kim, N. Y. Ha, J. Seidel, N. Park, J. S. Yun, J. H. Kim, Device design rules and operation principles of high-power perovskite solar cells for indoor applications. *Nano Energy* **68**, 104321 (2020).
9. D. M. Bishop, T. Todorov, Y. S. Lee, O. Gunawan, R. Haight, Record efficiencies for selenium photovoltaics and application to indoor solar cells, in *IEEE Photovoltaic Specialist Conference (PVSC)* (IEEE, 2017).
10. M. Zhu, G. Niu, J. Tang, Elemental Se: Fundamentals and its optoelectronic applications. *J. Mater. Chem. C* **7**, 2199–2206 (2019).
11. M. Feng, S.-C. Liu, L. Hu, J. Wu, X. Liu, D.-J. Xue, J.-S. Hu, L.-J. Wan, Interfacial strain engineering in wide-bandgap GeS thin films for photovoltaics. *J. Am. Chem. Soc.* **143**, 9664–9671 (2021).
12. M. Feng, C. Zuo, D.-J. Xue, X. Liu, L. Ding, Wide-bandgap perovskites for indoor photovoltaics. *Sci. Bull.* **66**, 2047–2049 (2021).
13. T. H. Youngman, R. Nielsen, A. Crovetto, B. Seger, O. Hansen, I. Chorkendorff, P. C. K. Vesborg, Semitransparent selenium solar cells as a top cell for tandem photovoltaics. *Sol. RRL* **5**, 2100111 (2021).
14. M. Freitag, J. Teuscher, Y. Saygili, X. Zhang, F. Giordano, P. Liska, J. Hua, S. M. Zakeeruddin, J.-E. Moser, M. Grätzel, A. Hagfeldt, Dye-sensitized solar cells for efficient power generation under ambient lighting. *Nat. Photon.* **11**, 372–378 (2017).
15. H. Michaels, M. Rinderle, R. Freitag, I. Benesperi, T. Edvinsson, R. Socher, A. Gagliardi, M. Freitag, Dye-sensitized solar cells under ambient light powering machine learning: Towards autonomous smart sensors for the internet of things. *Chem. Sci.* **11**, 2895–2906 (2020).
16. Y. Cui, Y. Wang, J. Bergqvist, H. Yao, Y. Xu, B. Gao, C. Yang, S. Zhang, O. Inganäs, F. Gao, J. Hou, Wide-gap non-fullerene acceptor enabling high-performance organic photovoltaic cells for indoor applications. *Nat. Energy* **4**, 768–775 (2019).
17. M. A. Saeed, S. H. Kim, H. Kim, J. Liang, H. Y. Woo, T. G. Kim, H. Yan, J. W. Shim, Indoor organic photovoltaics: Optimal cell design principles with synergistic parasitic resistance and optical modulation effect. *Adv. Energy Mater.* **11**, 2003103 (2021).
18. C. Dong, X.-M. Li, C. Ma, W.-F. Yang, J.-J. Cao, F. Igbari, Z.-K. Wang, L.-S. Liao, Lycopene-based bionic membrane for stable perovskite photovoltaics. *Adv. Funct. Mater.* **31**, 2011242 (2021).
19. C.-H. Chen, Z.-H. Su, Y.-H. Lou, Y.-J. Yu, K.-L. Wang, G.-L. Liu, Y.-R. Shi, J. Chen, J.-J. Cao, L. Zhang, X.-Y. Gao, Z.-K. Wang, Full-dimensional grain boundary stress release for flexible perovskite indoor photovoltaics. *Adv. Mater.* **34**, 2200320 (2022).
20. K.-L. Wang, Y.-G. Yang, Y.-H. Lou, M. Li, F. Igbari, J.-J. Cao, J. Chen, W.-F. Yang, C. Dong, L. Li, R.-Z. Tai, Z.-K. Wang, Smelting recrystallization of $CsPbBrI_2$ perovskites for indoor and outdoor photovoltaics. *eScience* **1**, 53–59 (2021).
21. J.-F. Guillemoles, T. Kirchartz, D. Cahen, U. Rau, Guide for the perplexed to the Shockley–Queisser model for solar cells. *Nat. Photon.* **13**, 501–505 (2019).
22. J. Wu, S.-C. Liu, Z. Li, S. Wang, D.-J. Xue, Y. Lin, J.-S. Hu, Strain in perovskite solar cells: Origins, impacts and regulation. *Nat. Sci. Rev.* **8**, nwab047 (2021).
23. S.-C. Liu, Z. Li, Y. Yang, X. Wang, Y.-X. Chen, D.-J. Xue, J.-S. Hu, Investigation of oxygen passivation for high-performance all-inorganic perovskite solar cells. *J. Am. Chem. Soc.* **141**, 18075–18082 (2019).
24. J. Mort, Transient photoconductivity in trigonal selenium single crystals. *J. Appl. Phys.* **39**, 3543–3549 (1968).
25. T. Leijtens, G. E. Eperon, A. J. Barker, G. Grancini, W. Zhang, J. M. Ball, A. R. S. Kandada, H. J. Snaith, A. Petrozza, Carrier trapping and recombination: The role of defect physics in

enhancing the open circuit voltage of metal halide perovskite solar cells. *Energ. Environ. Sci.* **9**, 3472–3481 (2016).
26. A. Kiligaridis, P. A. Frantsuzov, A. Yangui, S. Seth, J. Li, Q. An, Y. Vaynzof, I. G. Scheblykin, Are shockley-read-hall and ABC models valid for lead halide perovskites? *Nat. Commun.* **12**, 3329 (2021).
27. I. Hadar, X. Hu, Z.-Z. Luo, V. P. Dravid, M. G. Kanatzidis, Nonlinear band gap tunability in selenium–tellurium alloys and its utilization in solar cells. *ACS Energy Lett.* **4**, 2137–2143 (2019).
28. J. G. A. Speight, *Lange's Handbook of Chemistry* (McGraw Hill Book Co., 2005).
29. S.-C. Liu, C.-M. Dai, Y. Min, Y. Hou, A. H. Proppe, Y. Zhou, C. Chen, S. Chen, J. Tang, D.-J. Xue, E. H. Sargent, J.-S. Hu, An antibonding valence band maximum enables defect-tolerant and stable GeSe photovoltaics. *Nat. Commun.* **12**, 670 (2021).
30. A. Aslam, U. Mehmood, M. H. Arshad, A. Ishfaq, J. Zaheer, A. Ul Haq Khan, M. Sufyan, Dye-sensitized solar cells (DSSCs) as a potential photovoltaic technology for the self-powered Internet of Things (IoTs) applications. *Sol. Energy* **207**, 874–892 (2020).
31. Y. Cui, L. Hong, T. Zhang, H. Meng, H. Yan, F. Gao, J. Hou, Accurate photovoltaic measurement of organic cells for indoor applications. *Joule* **5**, 1016–1023 (2021).
32. W. Lu, L. Z. Li, M. Feng, H.-J. Yan, B. Yan, L. Hu, X. Zhang, S. Liu, J.-S. Hu. D.-J. Xue, Melt- and air-processed selenium thin-film solar cells. *Sci. China Chem.* (2022).
33. S. Biswas, H. Kim, Solar cells for indoor applications: Progress and development. *Polymers* **12**, 1338 (2020).
34. S. T. Pantelides, Defect dynamics and the Staebler-Wronski effect in hydrogenated amorphous silicon. *Phy. Rev. B* **36**, 3479–3482 (1987).
35. Y. Deng, S. Xu, S. Chen, X. Xiao, J. Zhao, J. Huang, Defect compensation in formamidinium–caesium perovskites for highly efficient solar mini-modules with improved photostability. *Nat. Energy* **6**, 633–641 (2021).
36. S. Chen, Y. Deng, H. Gu, S. Xu, S. Wang, Z. Yu, V. Blum, J. Huang, Trapping lead in perovskite solar modules with abundant and low-cost cation-exchange resins. *Nat. Energy* **5**, 1003–1011 (2020).
37. W. Chen, Y. Zhu, J. Xiu, G. Chen, H. Liang, S. Liu, H. Xue, E. Birgersson, J. W. Ho, X. Qin, J. Lin, R. Ma, T. Liu, Y. He, A. M.-C. Ng, X. Guo, Z. He, H. Yan, A. B. Djurišić, Y. Hou, Monolithic perovskite/organic tandem solar cells with 23.6% efficiency enabled by reduced voltage losses and optimized interconnecting layer. *Nat. Energy* **7**, 229–237 (2022).
38. I. Mathews, S. N. R. Kantareddy, S. Sun, M. Layurova, J. Thapa, J.-P. Correa-Baena, R. Bhattacharyya, T. Buonassisi, S. Sarma, I. M. Peters, Self-powered sensors enabled by wide-bandgap perovskite indoor photovoltaic cells. *Adv. Funct. Mater.* **29**, 1904072 (2019).
39. Y. Peng, T. N. Huq, J. Mei, L. Portilla, R. A. Jagt, L. G. Occhipinti, J. L. MacManus-Driscoll, R. L. Z. Hoye, V. Pecunia, Lead-free perovskite-inspired absorbers for indoor photovoltaics. *Adv. Energy Mater.* **11**, 2002761 (2021).
40. J. T. Heath, J. D. Cohen, W. N. Shafarman, Bulk and metastable defects in $CuIn_{1-x}Ga_xSe_2$ thin films using drive-level capacitance profiling. *J. Appl. Phys.* **95**, 1000–1010 (2004).
41. G. Kresse, J. Furthmüller, Efficient iterative schemes for ab initio total-energy calculations using a plane-wave basis set. *Phy. Rev. B* **54**, 11169–11186 (1996).
42. J. P. Perdew, A. Ruzsinszky, G. I. Csonka, O. A. Vydrov, G. E. Scuseria, L. A. Constantin, X. Zhou, K. Burke, Restoring the density-gradient expansion for exchange in solids and surfaces. *Phy. Rev. Lett.* **100**, 136406 (2008).

Acknowledgments
Funding: This work was supported by the National Natural Science Foundation of China (21922512 and 21875264) and the Youth Innovation Promotion Association CAS (Y2021014).
Author contributions: B.Y. and X.L. prepared films, fabricated devices, and characterized them. W.L., M.F., and H.-J.Y. assisted in the device characterization. Z.L. performed the DFT calculations and analyzed the results. S.L. and C.W. helped with the manuscript preparation. J.-S.H. and D.-J.X. wrote the paper. D.-J.X. supervised the project. All authors read and commented on the manuscript. **Competing interests:** The authors declare that they have no competing interests. **Data and materials availability:** All data needed to evaluate the conclusions in the paper are present in the paper and/or the Supplementary Materials.

Submitted 13 May 2022
Accepted 2 November 2022
Published 7 December 2022
10.1126/sciadv.adc9923